Supplementary Information (SI) for EES Catalysis.
This journal is © The Royal Society of Chemistry 2026

Supplementary Information

Cooperative Relay Catalysis over Cu-Fe Dual sites via N-Intermediate and Hydrogen Radical Pathways for Ammonia Production

Ming Zhang, [a] *Zhiguo Li,*[b] *Zhipeng Ma,**[a] *Constantine Tsounis,*[a] *Chen Han,*[a] *Shujie Zhou,*[a] *Wenyu Zhong,*[a] *Jitraporn Vongsvivut,*[c] *Jimmy Yun,*[a,d] *Zhe Weng,*[b] *Jian Pan,**[a] *and Rose Amal*[a]

[a] School of Chemical Engineering, The University of New South Wales, Kensington, New South Wales 2052, Australia

[b] Tianjin Key Laboratory of Advanced Carbon and Electrochemical Energy Storage, School of Chemical Engineering and Technology, and Collaborative Innovation Center of Chemical Science and Engineering, Tianjin University, Tianjin, 300072, China

[c] Infrared Microspectroscopy (IRM) Beamline, Australian Synchrotron, ANSTO, 800 Blackburn Road, Clayton, Victoria 3168, Australia

[d] Qingdao International Academician Park Research Institute, Qingdao, Shandong 266000, China

Corresponding author

Zhipeng Ma* E-mail: zhipeng.ma@unsw.edu.au

Jian Pan* E-mail: jian.pan@unsw.edu.au

1. Experimental Section

1.1. Electrochemical NO_3^-RR Experiment

1.1.1. Preparation of the Working Electrode

5.0 mg of the as-prepared catalysts were dispersed in a mixture of 500 µL of isopropanol, 450 µL Milli-Q water, 50 µL 5% Nafion 117 solution and sonicated for 30 min to form a uniform ink. 100 µL obtained ink was dropped on 1 cm^2 of carbon fibre paper.

1.1.2. NO_3^-RR Experiments

The electrochemical NO_3^-RR experiments were conducted in a 3-electrode H-cell reactor filled with Ar-saturated 0.1 M KNO_3 (Sigma Aldrich, 99%) and 0.1 M KOH (Sigma Aldrich, 85%) solution (pH = 13.26). Pt foil and an Ag/AgCl (saturated KCl) electrode were used as counter and reference electrode, respectively. The working electrode and counter electrode were separated by an anion exchange membrane. Each sample was evaluated for 30 minutes before the liquid products were collected using Autolab potentiostat (PGSTA204) to supply potential. The potentials were converted into reversible hydrogen electrode (RHE) scale by the Nernst equation ($E_{RHE} = E_{Ag/AgCl} + E^0_{Ag/AgCl} + 0.059 \times pH$).

1.1.3. Quantification of Products

Ammonia concentration was quantified by the standard indophenol-blue method. The resulting catholyte (500 μL) was transferred into a vial and sequentially mixed with the following solutions: (1) 400 μL of 1 M NaOH (Sigma Aldrich, 98%) containing 5 *wt*% salicylic acid (Sigma Aldrich, 99%) and 5 *wt*% sodium citrate (Sigma Aldrich, 99%), (2) 100 μL of 0.05 M NaClO (Sigma Aldrich, 99.9%), and (3) 30 μL of 1 *wt*% sodium nitroferricyanide solution (Sigma Aldrich, 99%). The mixture was thoroughly sonicated and kept in darkness at 25 °C for 2 hours. Subsequently, UV-vis spectroscopy of the resulting solution was recorded within the wavelength range of 550 to 800 nm. Using the peak absorbance around 653 nm, the NH_4^+ concentration was calculated based on calibration results obtained using standard solutions containing the specified NH_4Cl (Sigma Aldrich, 99.5%) concentrations.

Nitrite (NO_2^-) was quantified by the Griess Reagent method. In detail, 50 μL of the resulting catholyte was combined with Griess Reagent (50 μL) and Milli-Q water (900 μL) in a vial. The mixture was kept in darkness at 25 °C for 0.5 hours, after which the concentration of NO_2^- was determined through UV-vis spectroscopy of the solution. Using the peak absorbance around 525 nm, the NO_2^- concentration was calculated based on calibration results obtained using standard solutions containing the specific KNO_2 (Sigma Aldrich, 99%) concentrations.

The gas-phase products were analysed by a gas chromatograph (GC; GC-2010, Shimazu) equipped with TCD and FID detectors.

1.1.4. Calculation of Faradaic Efficiency

The Faradaic efficiency (FE) of products from te NO_3^-RR was calculated by the equation of $FE = \frac{N \times F \times C \times V}{Q} \times 100\%$, where N represents the number of e^- required for the formation of the selected product from NO_3^-RR ($N = 8$ for NH_4^+, $N = 2$ for NO_2^-), F denotes the Faraday constant ($F = 96485.33$), C stands for the measured molar concentration of the product via the UV-vis method, V signifies volume of the catholyte (50 mL), and Q indicates the total charge recorded during the experiment.

1.2. Characterization Methods

The morphology of the electrocatalysts was characterised using scanning electron microscopy (SEM, FEI Nova NanoSEM450 operated at 5 kV). The morphology and crystal structure, and elemental distribution of catalyst were analysed by transmission electron microscopy (TEM, JEOL JEM-F200 Multi-Purpose FEG-S/TEM, and SPECTRA 300S/TEM, FEI). The crystal structure was studied by X-ray diffraction (XRD) of powder samples and thin-film samples

collected on a PANalytical Xpert Multipurpose X-ray Diffraction System (MPD) with Cu Kα radiation (λ = 0.15406 nm) at 45kV and 40 mA with a scan rate of 5° min^{-1} from 5°–100° of 2θ. The Raman spectra were obtained using a Renishaw inVia microscope equipped with a 514 nm laser diode as the excitation source. X-ray photoelectron spectroscopy (XPS) utilised a monochromated Al Kα radiation source (1486.68 eV) to explore the surface chemical states of catalysts. Calibration of binding energy values in XPS spectra was performed using the C 1s peak at 284.8 eV. Cu/Fe K-edge XAS experiments were performed at the XAS beamline (MEX1) at the medium energy X-ray beamline at the Australian Synchrotron, Victoria, Australia. The k^2-weighted extended X-ray absorption fine structure (EXAFS) spectra were acquired by subtracting the post-edge background from the overall absorption and then normalising it to the edge-jump step. Subsequently, the Artemis program was used to carry out the least-squares curve fitting analysis of the EXAFS $\chi(k)$ data, and all fits were performed in the *R* space with *k*-weight of 2. Cu foil and Fe foil were employed to determine the amplitude reduction factor (S_0^2), which was held as the constant for the analysis of CuFe DACs. The EXAFS *R*-factor, indicating the percentage misfit of the theory to the data, was utilised to reveal the goodness of the fitting.

For electrochemical characterisations, the linear sweep voltammetry (LSV) was collected between 0.48 and −1.02 V vs. RHE (V_{RHE}) at a scan rate of 10 mV s^{-1} for NO_3^-RR in Ar-saturated electrolyte containing 0.1 M KNO_3 and 0.1 M KOH, and between −0.58 to −1.22 V_{RHE} at same scan rate for the hydrogen evolution reaction (HER) in the Ar-saturated electrolyte containing 0.1 M KCl (Sigma Aldrich, 99%) and 0.1 M KOH. The electrochemical impedance spectroscopy (EIS) was performed in Ar-saturated 0.1 M KNO_3 and 0.1 M KOH with frequency range of 0.1–100000 Hz for CuFe DACs and Cu SACs, and of 0.01–100000 Hz for Fe SACs with applied potential of −0.12 V_{RHE}. The double layer capacitance (C_{dl}) and ECSA of catalyst cathodes were measured by recording cyclic voltammetry (CV) curves in Ar-saturated 0.1 M KNO_3 and 0.1 M KOH solution. The CV curves were acquired at the non-faradaic potential range from 0.38–0.28 V_{RHE}, at different scan rates (V_b) of 4, 8, 16, 20, and 24 mV s^{-1}. Then the double-layer capacitance (C_{dl}) was estimated by plotting the $\Delta j = j_a - j_c$ (a, anode; c, cathode) as a function of the scan rate. It can be calculated using the equation of $C_{dl} = d(\Delta j)/2dV_b$. To extract the apparent activation energy E_a for NO_3^-RR, the catalyst electrochemical measurements were conducted in a 0.1 M KOH solution containing 0.1 M KNO_3 at different temperatures *i.e.,* 25, 30, 35, 40, 45 °C at −0.62 V_{RHE}. For heterogeneous electrocatalytic reactions, $j_{NH_4^+}$ can be expressed as a function of E_a according to equation of

$j = A_a \exp\left(-\frac{E_a}{RT}\right)$, where A_a is the apparent pre-exponential factor, R is the ideal gas constant (8.314 J K^{-1} mol^{-1}), and T is the temperature (K). Therefore E_a can be further calculated by fitting the slope of the Arrhenius plot according to the equation of $\left|\frac{\partial(\log j)}{\partial \frac{1}{T}}\right|_\eta = -\frac{E_a}{2.303R}$, where the intercept of log j vs. T^{-1} plot is the logarithm of A_a, And E_a = Slope × 2.303 × 8.314 [1-3]. Temperature control was achieved using an H-type electrochemical cell with a glass outer wall, which was continuously circulated with water from a thermostated water bath. The water was pumped from the bath into the cell jacket and returned to the bath to maintain thermal equilibrium. The electrolyte temperature inside the H-cell was monitored using a thermometer and allowed to stabilize at the target temperature before electrochemical measurements were initiated. This setup ensures reliable and consistent temperature control throughout the experiments.

Steady state j chronoamperometry was conducted in 0.10 M KOH electrolyte containing various concentrations of KNO_3 ranging from 0, 2.5×10^{-3}, 5.0×10^{-3}, 1.0×10^{-2}, 2.0×10^{-2}, 5.0×10^{-2} and 0.10 mol L^{-1}. The reaction order was determined from the slope of the log(j)-log(C_{NO3^-}) plot. All concentrations except 0 mol L^{-1} were included in the fitting interval, as the 0 mol L^{-1} point cannot be used for log-based analysis. Steady-state conditions were distinguished from transient behavior by allowing the current to stabilize for at least 50 s, after which the deviation of the current density was less than 2% of the final value. Under these conditions, the extracted slope of the log(j)-log(C_{NO3^-}) plot reflects the apparent reaction order.

Samples for the ^{1}H NMR experiments were prepared by mixing 2 mL of spent electrolyte and 2 mL of deionised water, which was further dissociated by 20 µL H_2SO_4 (Sigma Aldrich, 98%). Then 630 µL solution and 70 µL of D_2O (Sigma Aldrich, 99.9%) were loaded on an NMR tube and analysed by nuclear magnetic resonance (Avance III 600 MHz NMR, Bruker) using a pre-saturation method for water suppression.

The electron paramagnetic resonance spectroscopy (EPR) was collected using Bruker EMX X-Band ESR Spectrometer at room temperature. The EPR liquid samples were obtained by adding 12.5 mg of DMPO (12.3 µL at 25 ℃) into 0.4 mL of fresh electrolyte after 3-mintue NO_3^-RR at –0.62 V_{RHE}.

The *in-situ* FTIR experiments were carried out using the Infrared Microspectroscopy (IRM) Beamline at the Australian Synchrotron, Melbourne, Australia. The IRM beamline combines

the high brilliance and high collimation of the synchrotron beam with a Bruker V80v FTIR spectrometer and a Hyperion 2000 IR microscope to reach high signal-to-noise ratios at diffraction limited spatial resolutions between 3 and 8 μm. This makes the beamline ideally suited to the analysis of microscopic samples. Both the microscope and the spectrometer were controlled via Bruker OPUS software, version 7.2, including data acquisition, sample stage position and automated multipoint data collection. Measurements were performed using a narrow-band, high-sensitivity, liquid nitrogen-cooled Mercury Cadmium Telluride (MCT) detector. It was optimised for detection and data collection at a wavelength range of 3800–900 cm^{-1}. The aperture was set to ~10 μm × 10 μm. A custom-designed stationary three-electrode electrochemical cell was employed, featuring a 2 cm diameter ZnSe window positioned directly above the working electrode (catalyst coated onto carbon paper). An Ag/AgCl electrode and a Pt wire were used as the reference and counter electrodes, respectively. The cell was filled with 2 mL of Ar-saturated electrolyte (0.1 M KNO_3 and 0.1 M KOH). Prior to electrochemical testing, the background FTIR spectrum was collected under open-circuit conditions (OCC) without applying any external potential. Potential-dependent FTIR measurements were subsequently carried out, applying potentials from open-circuit to −0.62 V_{RHE}. Spectra were recorded at selected potentials (−0.02 V_{RHE}, −0.22 V_{RHE}, −0.42 V_{RHE}, and −0.62 V_{RHE}). At least four independent scans were collected at each potential to ensure effective signal collection. Each spectrum was acquired in reflection mode, averaging 256 scans per measurement, with a spectral resolution of 2 cm^{-1}.

1.3. Computational Methods

The first-principles calculations were performed using the VASP software package [4-6]. The exchange-correlation potential was treated within the generalised gradient approximation (GGA) using the Perdew-Burke-Ernzerhof (PBE) formulation [7,8]. The electron-ion interaction was described by the projector augmented wave (PAW) method [9]. The cutoff energy for the plane-wave basis set was set to 450 eV. All structures were geometrically optimised until the maximum component of the forces was less than 0.01 eV $Å^{-1}$. Integration over the Brillouin zone was performed using the Monkhorst-Pack grid, with a k-point grid set to 3 × 3 × 1. The formula used to calculate the Gibbs free energy is G = E + ZPE - TS, where E is the energy directly obtained from DFT calculations, ZPE represents the zero-point energy, T is the temperature, and S is the entropy of the system. The change in Gibbs free energy ΔG for a reaction is equal to the sum of the Gibbs free energies of the products minus the sum of the Gibbs free energies of the reactants.

All models were visualised using VESTA [10].

2. Supplementary Figures and Tables

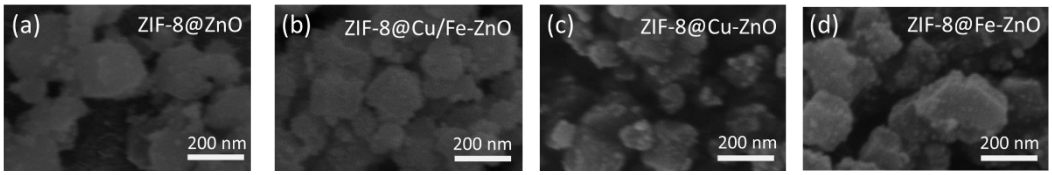

Figure S1. SEM images of (**a**) ZnO, (**b**) Cu/Fe-ZnO, (**c**) Cu-ZnO, and (**d**) Fe-ZnO coverages on ZIF-8.

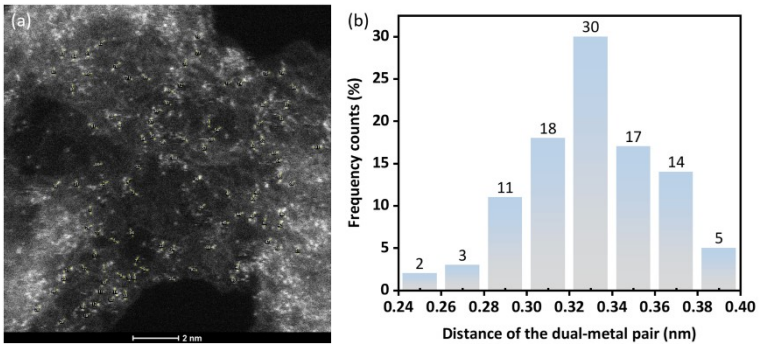

Figure S2. (**a**) The AC HAADF-STEM image of CuFe DACs and (**b**) statistical analysis on the nearest-neighbour distance distribution.

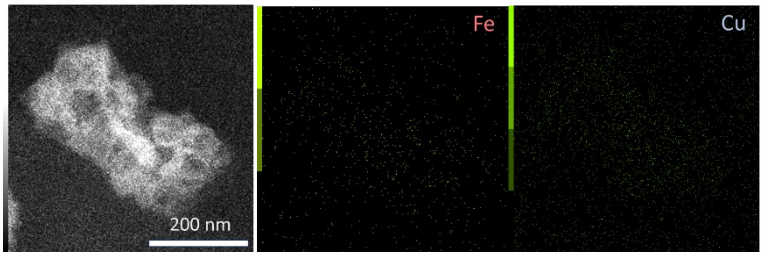

Figure S3. The metal elemental distribution of CuFe DACs in EDS mapping.

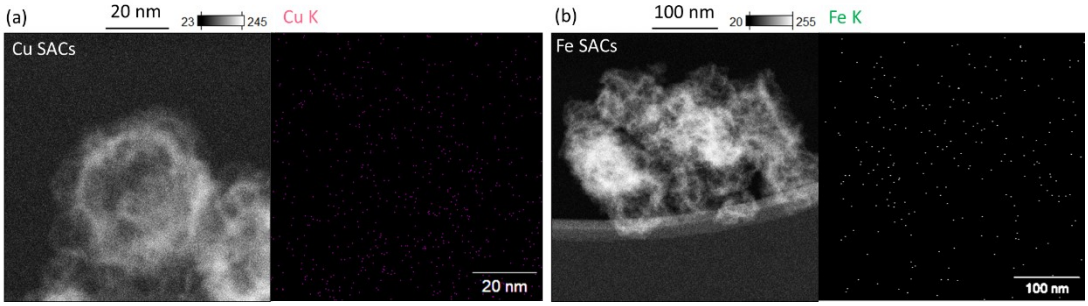

Figure S4. The metal elemental distribution of (**a**) Cu SACs and (**b**) Fe SACs in EDS mapping.

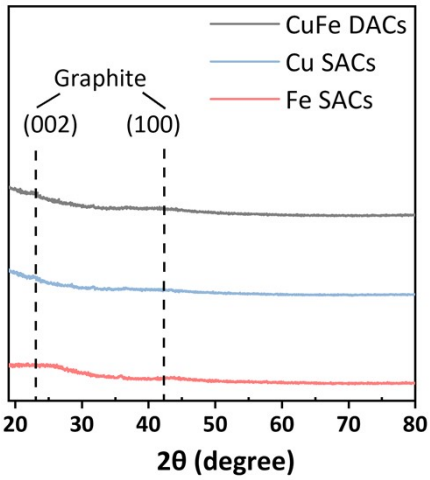

Figure S5. XRD pattern of CuFe DACs, Cu SACs, and Fe SACs.

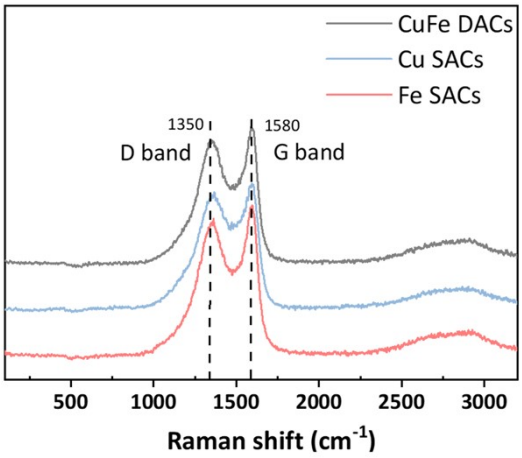

Figure S6. Raman spectrum of CuFe DACs, Cu SACs, and Fe SACs.

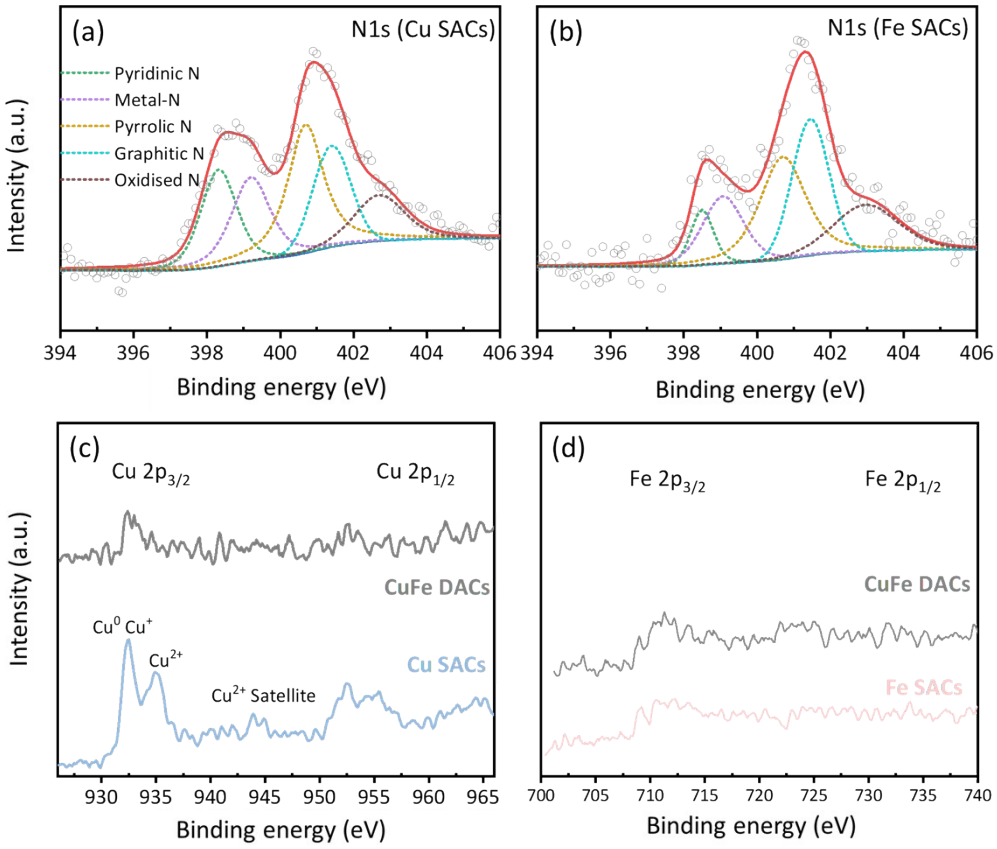

Figure S7. N 1s XPS spectrum of (**a**) Cu SACs, and (**b**) Fe SACs. (**c**) Cu 2p XPS spectrum of CuFe DACs and Cu SACs. (**d**) Fe 2p XPS spectrum of CuFe DACs and Fe SACs.

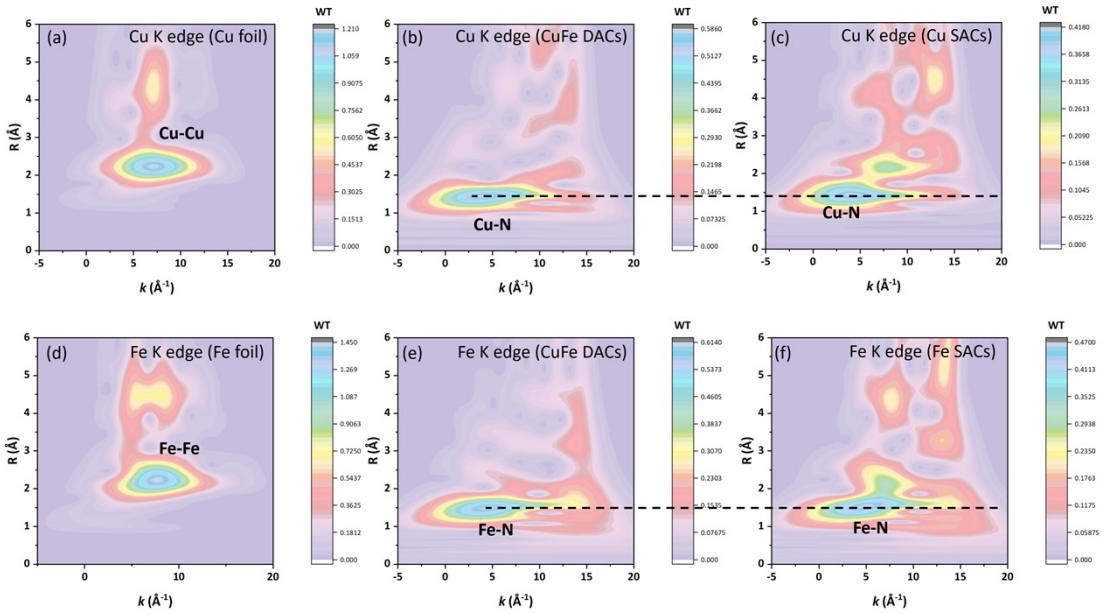

Figure S8. WT-EXAFS of (**a**) Cu foil, (**b**) CuFe DACs, (**c**) Cu SACs at Cu K-edge, and (**d**) Fe foil, (**e**) CuFe DACs, (**f**) Fe SACs at Fe K-edge.

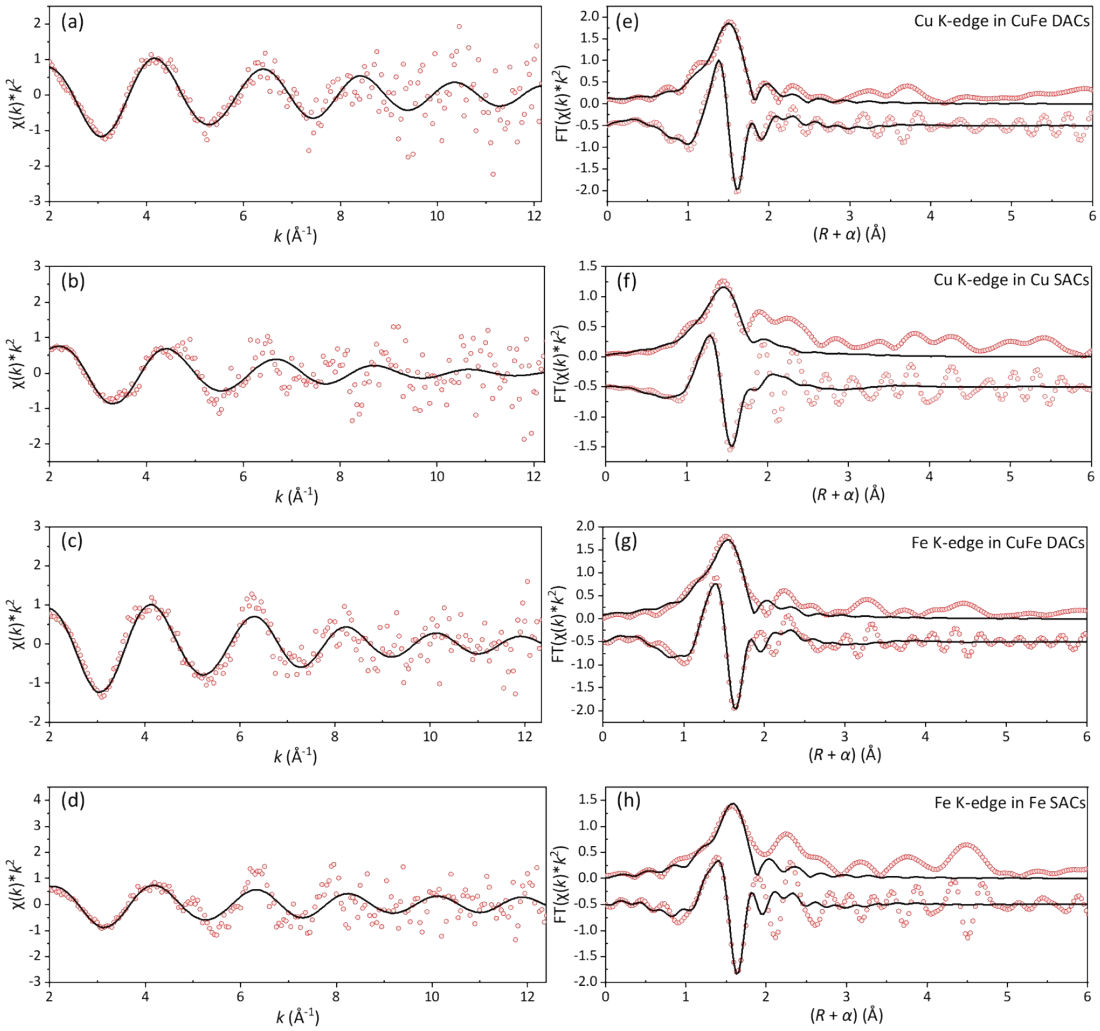

Figure S9. Cu K-edge EXAFS (point) and the curve fit (line) for (**a**) CuFe DACs and (**b**) Cu SACs. Fe K-edge EXAFS (point) and the curve fit (line) for (**c**) CuFe DACs and (**d**) Fe SACs, shown in k^2-weighted k-space. Cu K-edge EXAFS (point) and the curve fit (line) for (**e**) CuFe DACs and (**f**) Cu SACs. Fe K-edge EXAFS (point) and the curve fit (line) for (**g**) CuFe DACs and h) Fe SACs, shown in R-space (FT magnitude and imaginary component). The data are k^2-weighted and not phase-corrected.

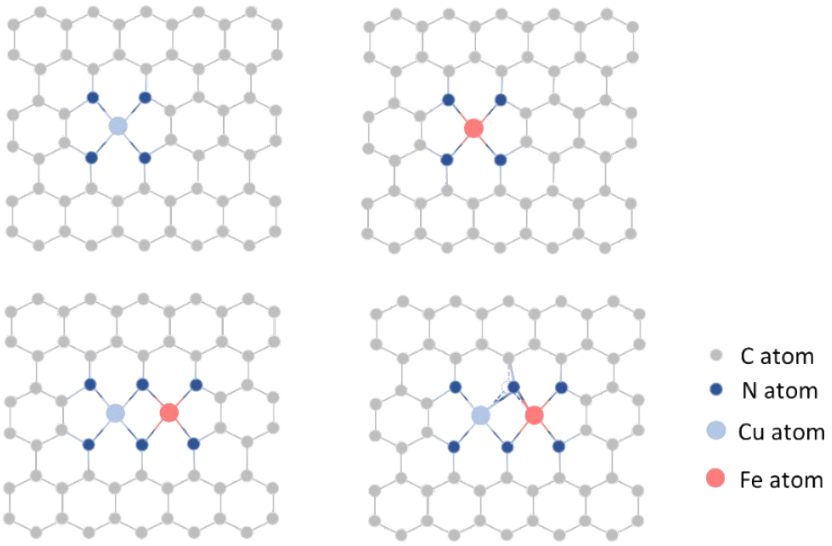

Figure S10. DFT modelling of surface on Cu SACs, Fe SACs, ideal CuFe DACs, and CuFe DACs after structural relaxation.

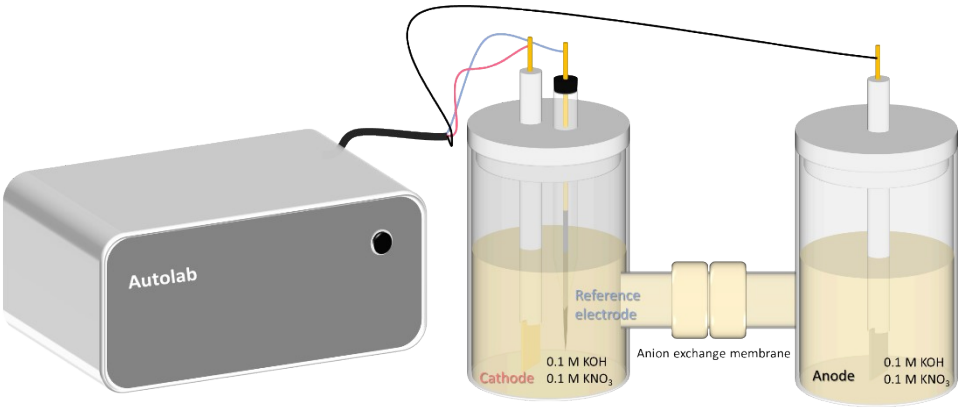

Figure S11. The set-up of H-cell for electrochemical NO_3^- reduction reaction.

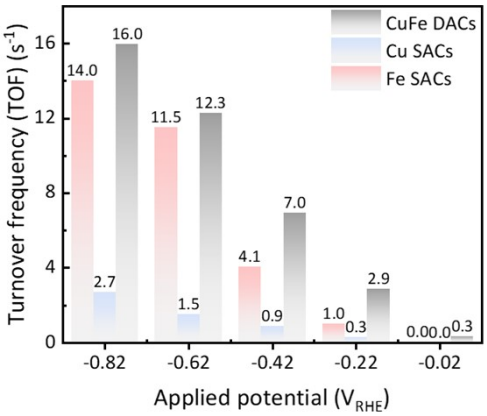

Figure S12. Potential-dependent turnover frequencies (TOFs) for nitrate-to-ammonium conversion over the three catalysts. The TOF values were calculated based on the metal contents determined by ICP–OES, assuming that all metal atoms are catalytically accessible. TOF is defined as the number of product molecules generated per active site per second. For CuFe

DACs, the maximum TOF was additionally calculated by assuming that each Cu–Fe pair acts as a single active site, following the equation ($\mathrm{TOF}_{\mathrm{pair}} = \frac{r_{\mathrm{product}}\,(mol/s)}{n_{\mathrm{pair}}\,(mol)}$).

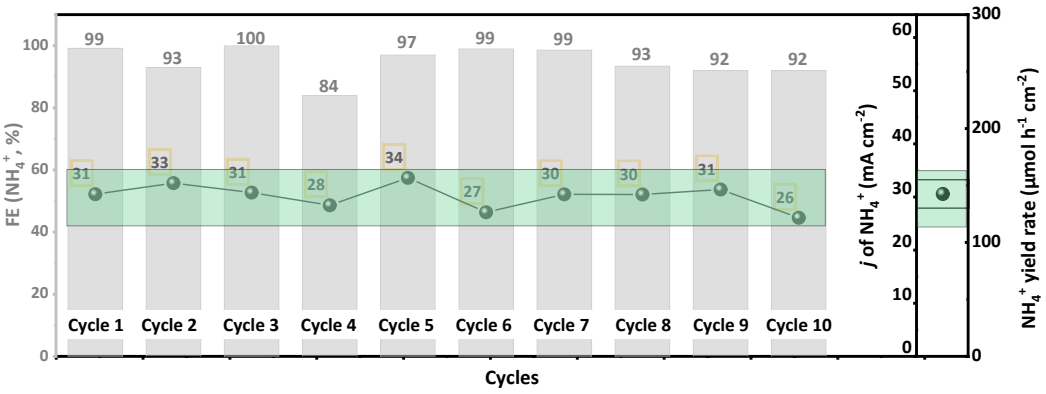

Figure S13. Durability test of CuFe DACs in NO_3^-RR at −0.62 V_{RHE} with 10 cycles (0.5 h for each cycle) for FE, partial current density (j), yield rate towards NH_4^+.

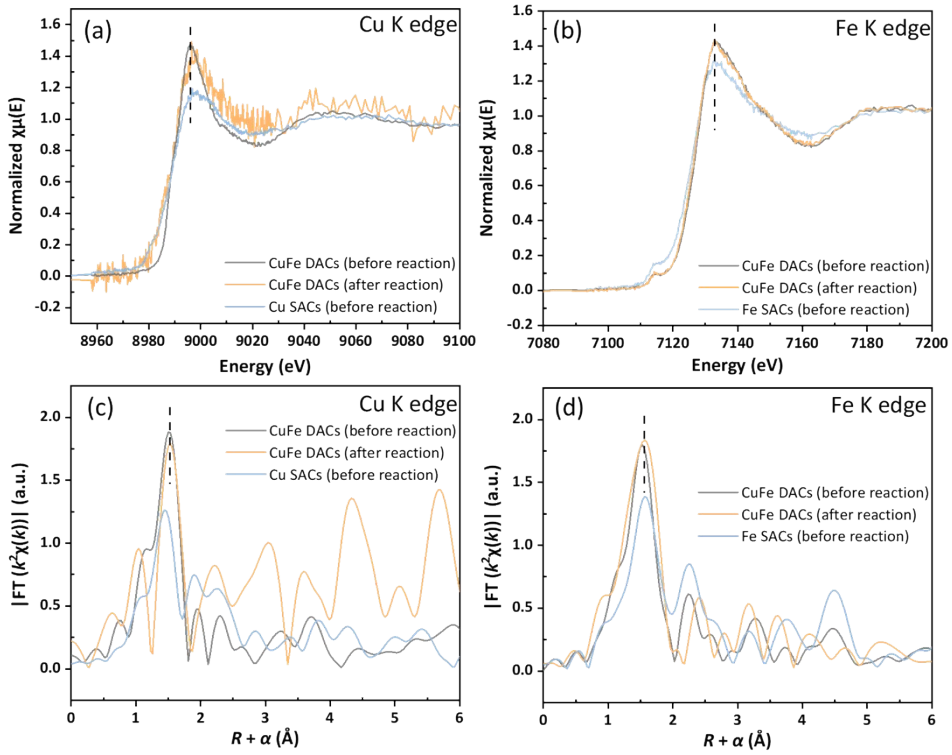

Figure S14. (**a**) Cu K-edge XANES for CuFe DACs before NO_3^-RR, after NO_3^-RR, and Cu SACs before NO_3^-RR. (**b**) Fe K-edge XANES for CuFe DACs before NO_3^-RR, after NO_3^-RR, and Fe SACs before NO_3^-RR. (**c**) Cu K-edge FT-EXAFS for before NO_3^-RR, after NO_3^-RR, and Cu SACs before NO_3^-RR in R-space. (**d**) Fe K-edge FT-EXAFS for before NO_3^-RR, after

NO_3^-RR, and Cu SACs before NO_3^-RR in *R*-space (the data are k^2-weighted and not phase-corrected).

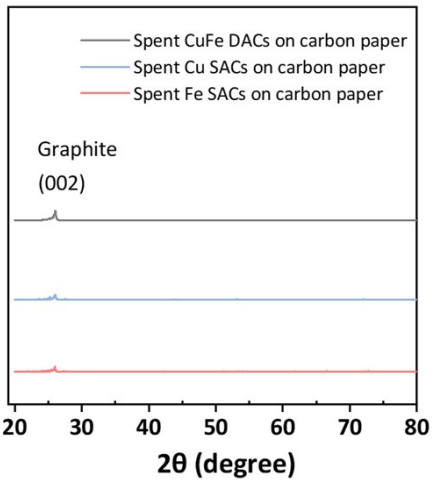

Figure S15. XRD pattern of CuFe DACs, Cu SACs, and Fe SACs on carbon paper after NO_3^-RR.

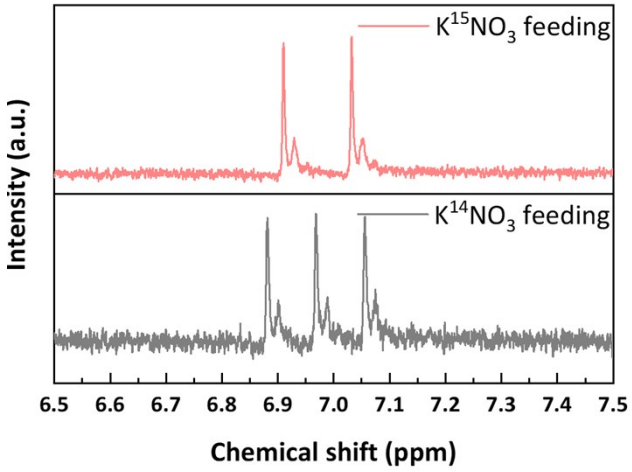

Figure S16. ^{1}H NMR spectra of $^{15}NH_4^+$ and $^{14}NH_4^+$ produced after NO_3^-RR using $^{15}NO_3^-$ and $^{14}NO_3^-$ as reactants, respectively.

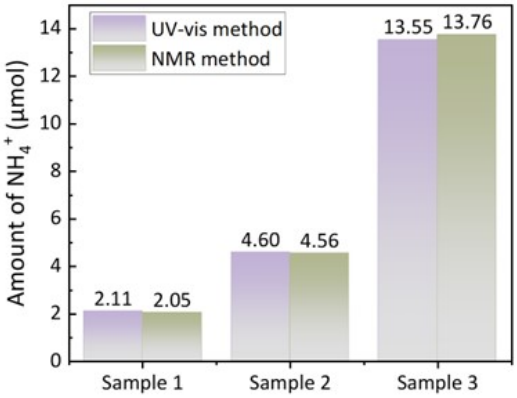

Figure S17. Comparison of NH_4^+ quantification by UV-vis method and NMR method.

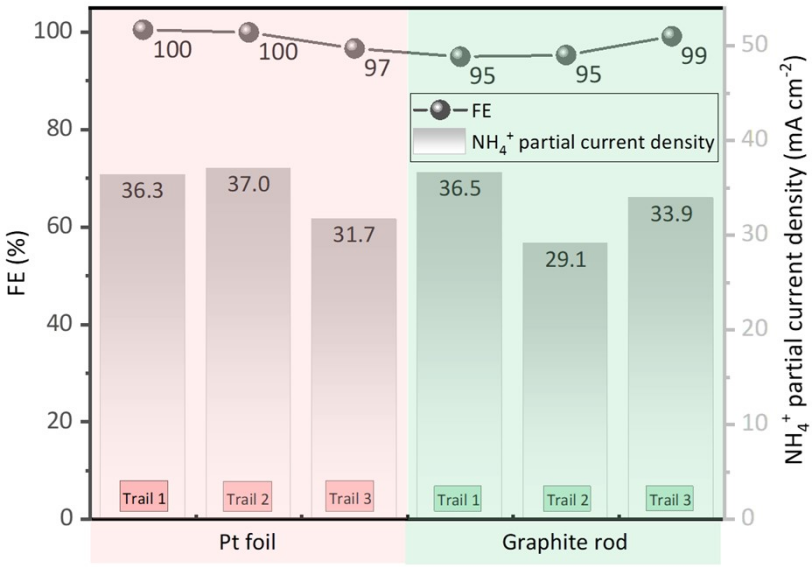

Figure S18. NO_3^-RR trails with different counter electrodes (Pt foil and graphite rod) at −1.6 V_{RHE}.

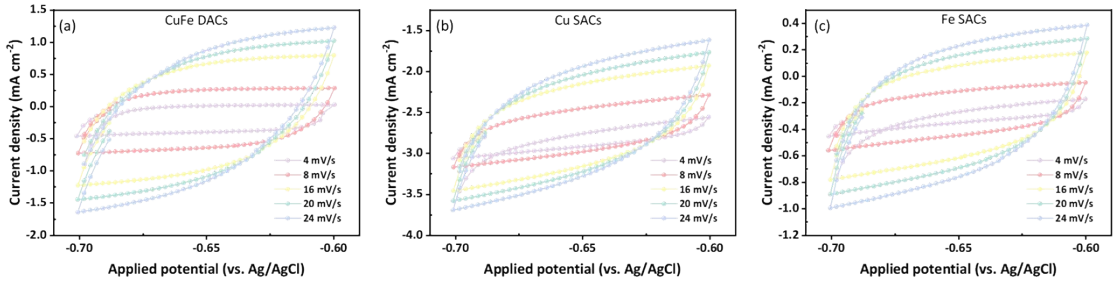

Figure S19. ECSA measurements of (**a**) CuFe DACs, (**b**) Cu SACs, and (**c**) Fe SACs.

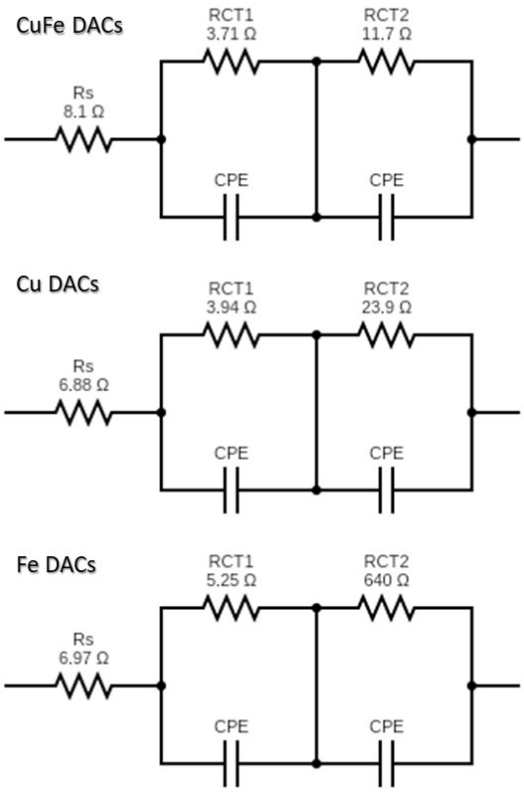

Figure S120. Equivalent circuit fitting results of EIS for CuFe DACs, Cu SACs, and Fe SACs (from top to bottom).

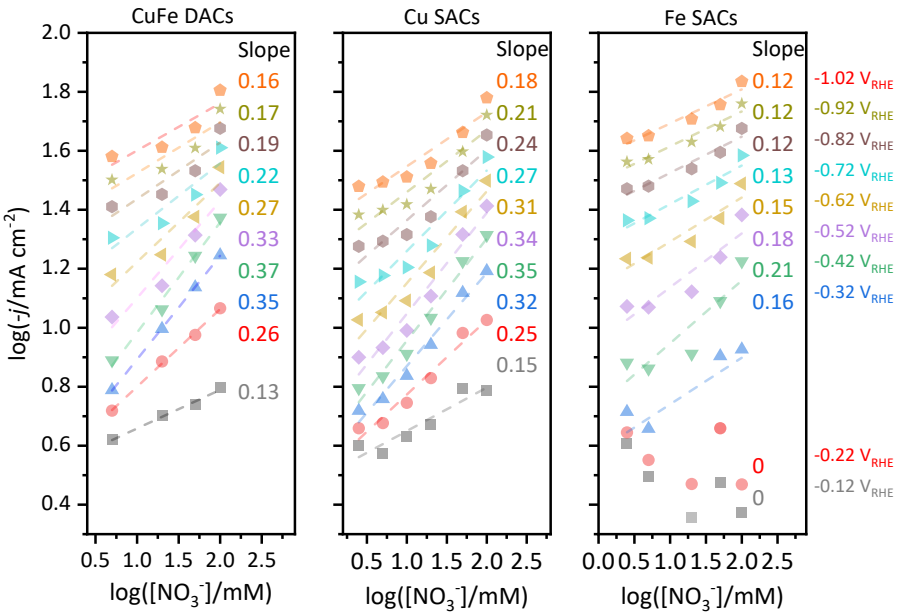

Figure S21. Log-log plot of current density versus NO_3^- concentration at various potentials. The slope of each fitted line represents the reaction rate order.

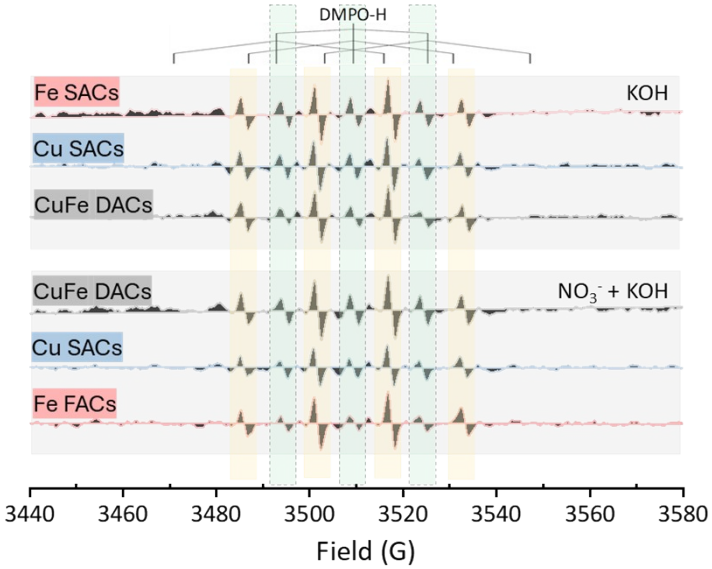

Figure S22. EPR spectrum of the DMPO–H adduct. The yellow bars indicate regions of potential overlap with the DMPO–OH signal, while the green bars represent the characteristic peaks of DMPO–H with no interference from other radical species [11].

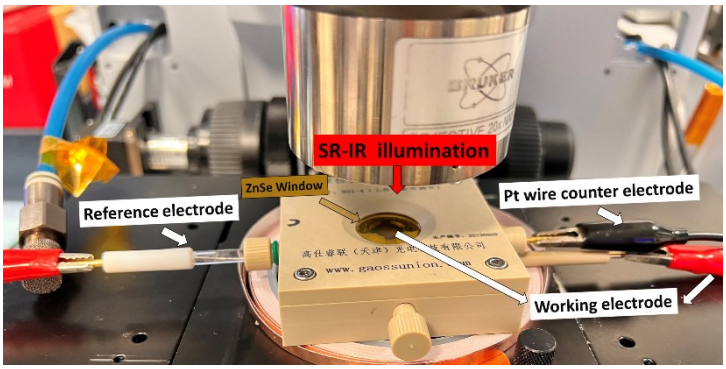

Figure S23. Setup employed for *in-situ* FTIR characterization in ANSTO, Australia.

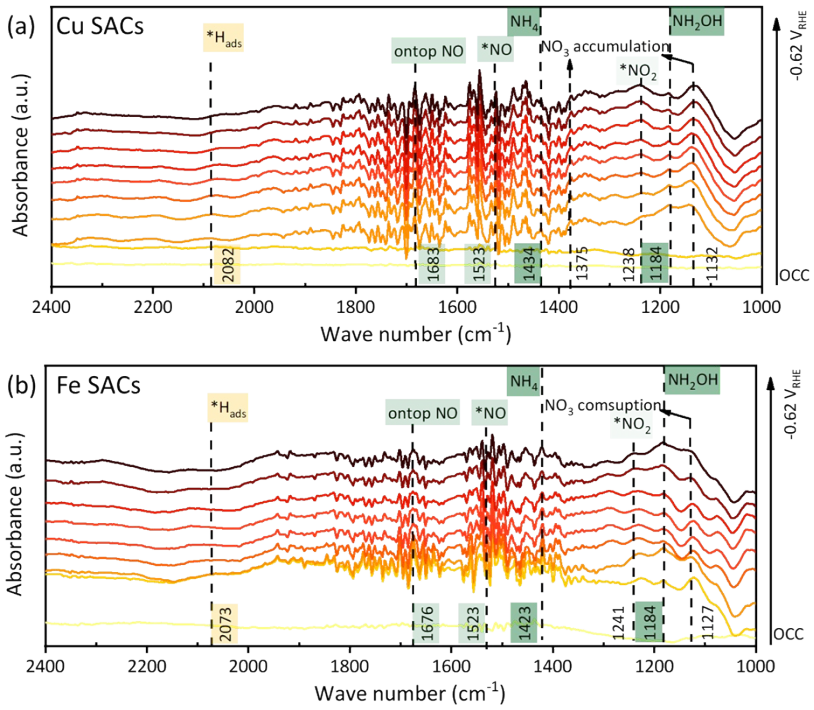

Figure S24. The *in-situ* FTIR spectrum of (**a**) Cu SACs and (**b**) Fe SACs in NO_3^-RR via chronoamperometry polarization.

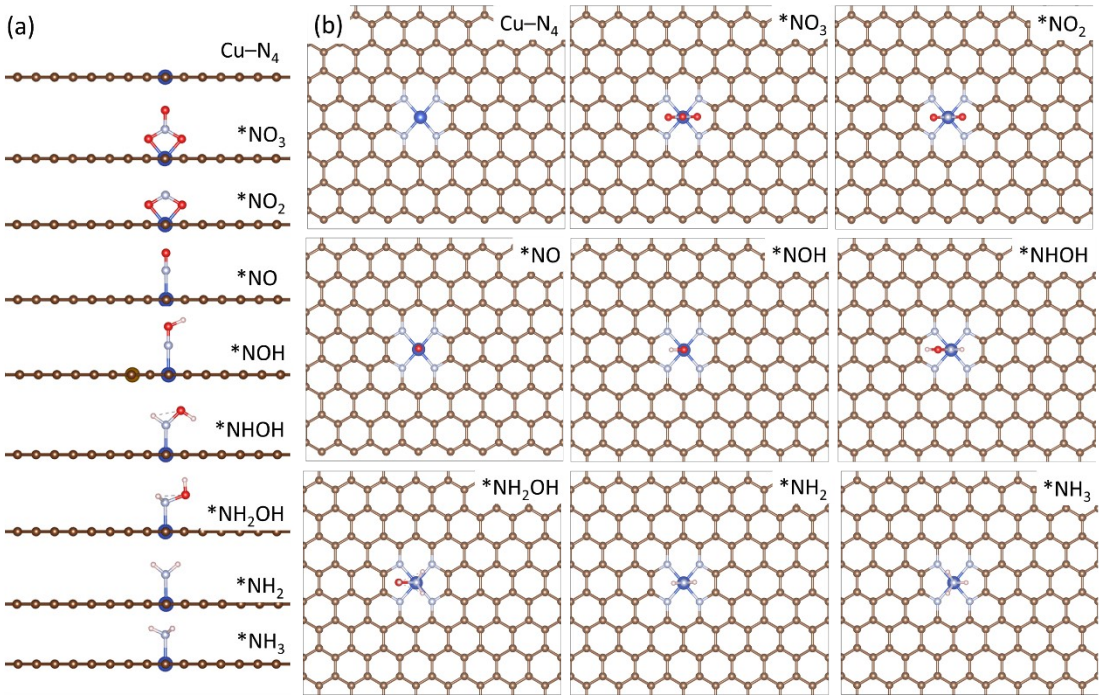

Figure S25. (**a**) The side views and (**b**) top views of all NO_3^-RR intermediates on metal sites of Cu–N_4. Blue, red, silver and pink balls represent Cu, O, N and H atoms, respectively.

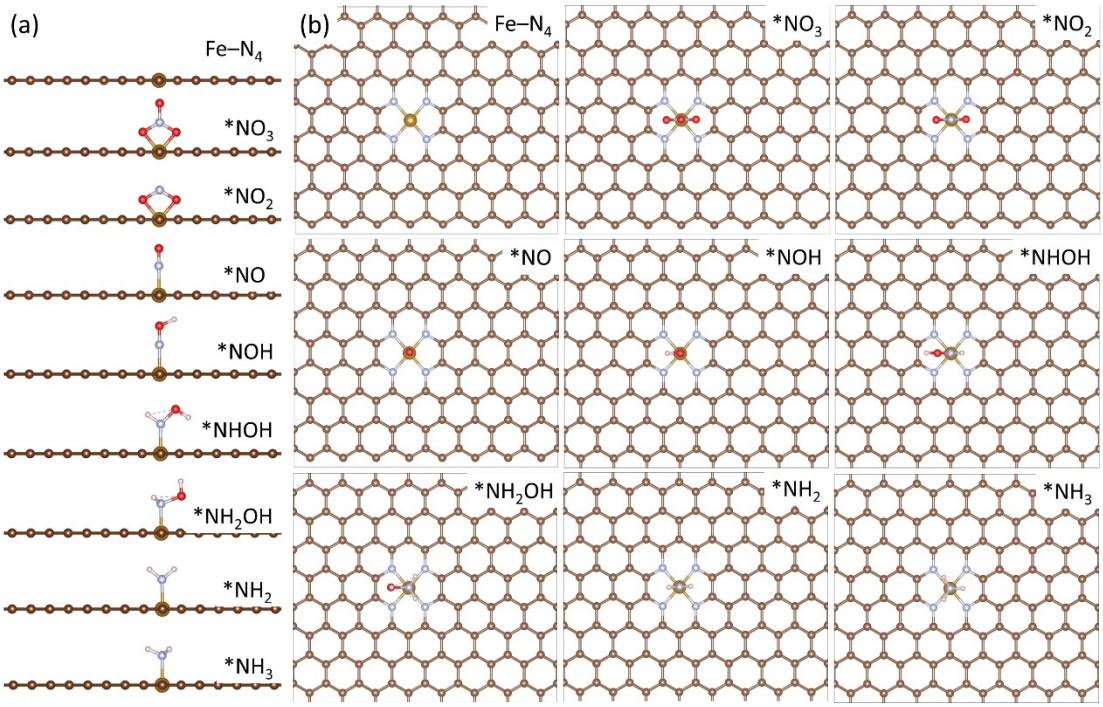

Figure S26. (**a**) The side views and (**b**) top views of all NO_3^-RR intermediates on metal sites of Fe–N_4. Brown, red, silver and pink balls represent Fe, O, N and H atoms, respectively.

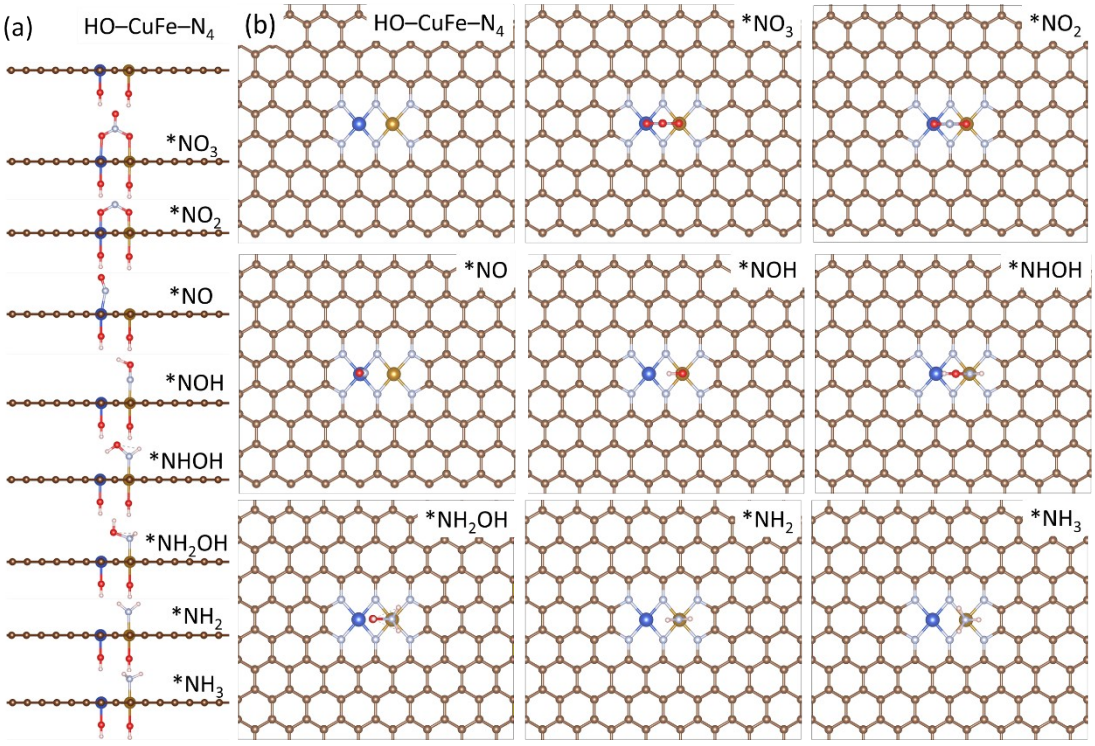

Figure S27. (**a**) The side views and (**b**) top views of all NO_3^-RR intermediates on metal sites of HO–CuFe–N_4. Blue, brown, red, silver and pink balls represent Cu, Fe, O, N and H atoms, respectively.

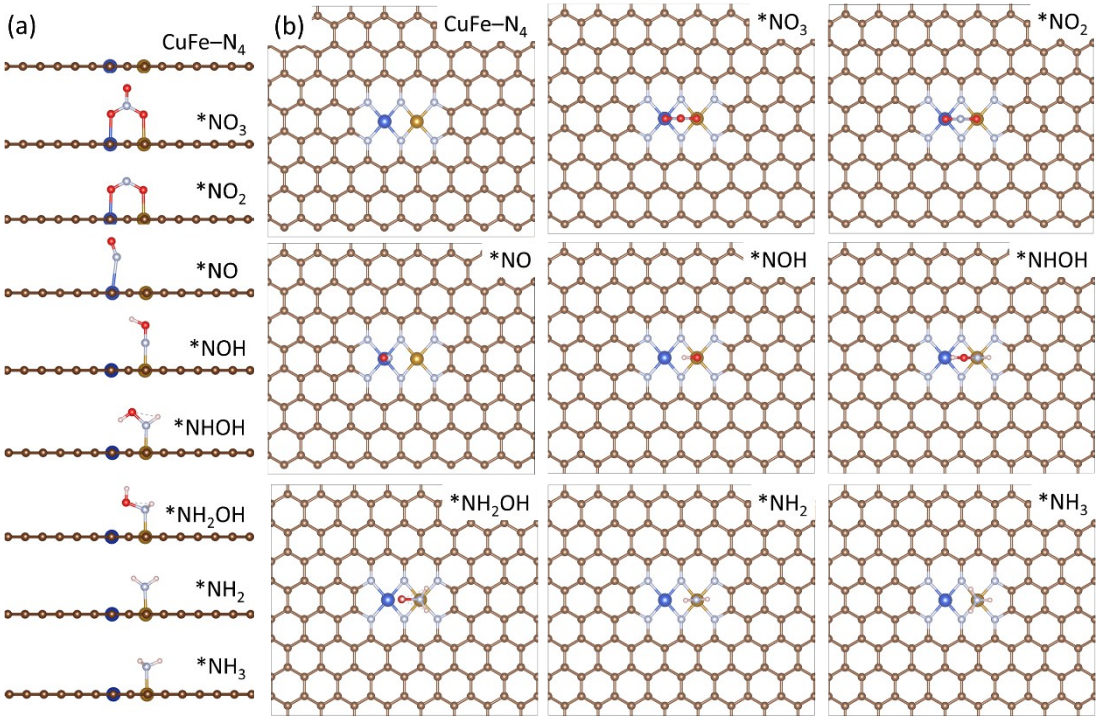

Figure S28. (**a**) The side views and (**b**) top views of all NO_3^-RR intermediates on metal sites of CuFe–N_4. Blue, brown, red, silver and pink balls represent Cu, Fe, O, N and H atoms, respectively.

Table S1. ICP-OES analysis on CuFe SACs, Cu SACs, and Fe SACs.

Samples [units][a)]	Cu (wt%)	Fe (wt%)
CuFe DACs	0.06	0.07
Cu SACs	0.25	-
Fe SACs	-	0.03

Table S2. N 1s XPS fitting parameters on CuFe SACs, Cu SACs, and Fe SACs.

Samples	The binding energy of each component peak (eV)	FWHM	Peak Area	Peak shape (%Lorentzian-Gaussian)	Background subtraction
CuFe DACs	398.4	0.95	386.3	23%	Shirley
	399.2	1.25	571.2	45%	
	400.5	1.37	1027.4	48%	
	401.3	1.36	885.7	7%	
	402.9	2.33	718.4	43%	
Cu SACs	398.3	1.15	503.0	30%	Shirley
	399.2	1.24	513.4	51%	
	400.7	1.15	801.1	76%	
	401.4	1.22	490.6	0%	
	402.7	1.63	341.5	32%	
Fe SACs	398.5	0.73	168.1	30%	Shirley
	399.1	1.32	368.1	29%	
	400.7	1.47	608.2	51%	
	401.5	1.18	586.8	0%	
	403.0	2.09	392.2	24%	

Table S3. k^2-weighted FT-EXAFS fitting results at the Cu/Fe K-edge of CuFe DACs, Cu SACs and Fe SACs samples.

Samples [a)]	First shell	Coordination number (CN)	R + ΔR (Å)	δ^2(Å^2)
CuFe DACs	Cu–N	4.84 ± 0.45	1.96 ± 0.004	0.002
	Fe–N	5.59 ± 0.83	2.02 ± 0.017	0.003
Cu SACs	Cu–N	3.75 ± 0.77	1.92 ± 0.025	0.006
Fe SACs	Fe–N	3.45 ± 0.56	2.03 ± 0.018	0.001

[a)] δ^2: Debye-Waller factors. The goodness of fit (*R* factor) for CuFe DACs (Cu K-edge), CuFe DACs (Fe K-edge), Cu SACs (Cu K-edge), and Fe SACs (Fe K-edge) are 0.0091, 0.0205, 0.01197, 0.0161, respectively. The obtained XAFS data was processed in Athena for background, pre/post-edge line calibration. The Fourier transformed fitting was carried out in Artemis. The weighting of 2, *k*-range of 2–12.151 Å^{-1} for CuFe DACs (Cu K-edge), 2–12.151 Å^{-1} for CuFe DACs (Fe K-edge), 2–12.151 Å^{-1} for Cu SACs (Cu K-edge), 2–12.151 Å^{-1} for Fe SACs (Fe K-edge), and *R* range of 1–2 Å for CuFe DACs (Cu/Fe K-edge), 1–1.84 Å for Cu SACs (Cu K-edge), and 1–1.87 Å for Fe SACs (Fe K-edge) were used for fitting. The amplitude reduction factor S_0^2 was defined at 0.907 for Cu K-edge and 0.792 for Fe K-edge obtained by the fitting result from standard Cu and Fe foil k^2-weighted FT-EXAFS spectra. Coordination number, bond length, Debye Waller factor, and E_0 (inner potential correction) shift (ΔE_0) were fitted without being fixed or constrained by anyone.

Table S4. Slopes in Figure 5a and Figure S16, and corresponding double-layer capacity (C_{dl}) with electrochemical active surface area (ECSA).

	Slope	C_{dl}	ECSA
CuFe SACs	0.0817	0.0408 F cm^{-2}	1021 cm^2
Cu SACs	0.0579	0.0289 F cm^{-2}	723.5 cm^2
Fe SACs	0.0451	0.0226 F cm^{-2}	564.1 cm^2

Table S5. Details of the reaction energy, zero-point energy, and entropy corrections of each intermediate in the free energy calculation.

Temperature (℃)	Temperature (K)	j_{NH4+} of CuFe DACs (mA cm^{-2})	j_{NH4+} of Cu SACs (mA cm^{-2})	j_{NH4+} of Fe SACs (mA cm^{-2})
25	298.15	19.19	23.13	16.87
30	303.15	29.85	24.43	26.20
35	308.15	32.69	28.28	23.47
40	313.15	37.45	30.35	24.73
45	318.15	36.85	35.31	26.83

Table S6. The partial current density of NH_4^+ (j_{NH4+}) in NO_3^-RR at different temperature among three catalysts.

	Gibbs energy (eV)	DFT energy (eV)	ZPE (eV)	T (K)	S (eV/K)	TS (eV)
HO–CuFe–N_4	-4370.86	-4371.06	2.36	300	0.00720	2.16
HO–CuFe–N_4-NO_3	-4397.31	-4398.00	2.89	300	0.00732	2.20
HO–CuFe–N_4-NO_2	-4391.29	-4391.77	2.66	300	0.00724	2.17
HO–CuFe–N_4-NO	-4383.39	-4383.72	2.49	300	0.00720	2.16
HO–CuFe–N_4-NOH	-4385.64	-4386.05	2.58	300	0.00724	2.17
HO–CuFe–N_4-NHOH	-4391.01	-4391.58	2.74	300	0.00726	2.18
HO–CuFe–N_4-NH_2OH	-4395.73	-4396.57	3.03	300	0.00728	2.18
HO–CuFe–N_4-NH_2	-4386.09	-4386.74	2.82	300	0.00722	2.17
HO–CuFe–N_4-NH_3	-4390.51	-4391.63	3.29	300	0.00723	2.17
CuFe–N_4	-4354.31	-4354.18	2.01	300	0.00713	2.14
CuFe–N_4-NO_3	-4380.23	-4380.60	2.55	300	0.00725	2.18
CuFe–N_4-NO_2	-4374.42	-4374.59	2.33	300	0.00717	2.15
CuFe–N_4-NO	-4366.63	-4366.64	2.15	300	0.00713	2.14
CuFe–N_4-NOH	-4368.39	-4368.47	2.24	300	0.00717	2.15
CuFe–N_4-NHOH	-4374.20	-4374.44	2.40	300	0.00719	2.16
CuFe–N_4-NH_2OH	-4378.75	-4379.28	2.69	300	0.00721	2.16
CuFe–N_4-NH_2	-4369.02	-4369.36	2.48	300	0.00715	2.15
CuFe–N_4-NH_3	-4374.08	-4374.88	2.94	300	0.00716	2.15
Cu–N_4	-4346.88	-4346.64	1.93	300	0.00721	2.16
Cu–N_4-NO_3	-4366.97	-4367.19	2.43	300	0.00734	2.20
Cu–N_4-NO_2	-4360.93	-4361.08	2.32	300	0.00725	2.18
Cu–N_4-NO	-4357.91	-4357.90	2.14	300	0.00721	2.16
Cu–N_4-NOH	-4360.13	-4360.19	2.23	300	0.00725	2.18
Cu–N_4-NHOH	-4365.48	-4365.68	2.39	300	0.00727	2.18
Cu–N_4-NH_2OH	-4370.09	-4370.59	2.68	300	0.00729	2.19
Cu–N_4-NH_2	-4359.99	-4360.29	2.47	300	0.00723	2.17
Cu–N_4-NH_3	-4365.57	-4366.33	2.93	300	0.00724	2.17
Fe–N_4	-4352.31	-4351.97	1.84	300	0.00729	2.19
Fe–N_4-NO_3	-4371.61	-4371.74	2.36	300	0.00742	2.23
Fe–N_4-NO_2	-4367.36	-4367.42	2.26	300	0.00733	2.20
Fe–N_4-NO	-4364.67	-4364.56	2.08	300	0.00729	2.19
Fe–N_4-NOH	-4366.38	-4366.35	2.17	300	0.00733	2.20
Fe–N_4-NHOH	-4372.22	-4372.35	2.33	300	0.00735	2.20

$Fe–N_4-NH_2OH$	-4376.52	-4376.97	2.66	300	0.00737	2.21
$Fe–N_4-NH_2$	-4367.06	-4367.30	2.44	300	0.00731	2.19
$Fe–N_4-NH_3$	-4371.89	-4372.60	2.91	300	0.00732	2.20
H_2	-06.75	-07.02	0.27	300	0.00000000	0.00000
H_2O	-14.21	-14.80	0.58	300	0.00000434	0.00130
NO_2	-17.68	-17.97	0.30	300	0.00003165	0.00949
NO_3	-23.06	-23.57	0.55	300	0.00011301	0.03390
NH_3	-19.51	-20.47	0.97	300	0.00002375	0.00712

Reference

1. Luo, W., Wu, S., Jiang, Y., Xu, P., Zou, J., Qian, J., Zhou, X., Ge, Y., Nie, H., and Yang, Z. (2023). Efficient Electrocatalytic Nitrate Reduction to Ammonia Based on DNA-Templated Copper Nanoclusters. ACS Appl. Mater. Interfaces *15*, 18928-18939. 10.1021/acsami.3c00511.
2. Zhou, N., Wang, Z., Zhang, N., Bao, D., Zhong, H., and Zhang, X. (2023). Potential-Induced Synthesis and Structural Identification of Oxide-Derived Cu Electrocatalysts for Selective Nitrate Reduction to Ammonia. ACS Catal. *13*, 7529-7537. 10.1021/acscatal.3c01315.
3. He, Q., Shen, Y., Li, R., Peng, T., Chen, N., Wu, Z., and Feng, C. (2022). Rice washing drainage (RWD) embedded in poly(vinyl alcohol)/sodium alginate as denitrification inoculum for high nitrate removal rate with low biodiversity. Bioresour. Technol. *355*, 127288. 10.1016/j.biortech.2022.127288.
4. Kresse, G., and Hafner, J. (1993). Ab initio molecular dynamics for liquid metals. Phys. Rev. B *47*, 558-561. 10.1103/PhysRevB.47.558.
5. Kresse, G., and Furthmüller, J. (1996). Efficiency of ab-initio total energy calculations for metals and semiconductors using a plane-wave basis set. Comput. Mater. Sci *6*, 15-50. 10.1016/0927-0256(96)00008-0.
6. Kresse, G., and Furthmüller, J. (1996). Efficient iterative schemes for ab initio total-energy calculations using a plane-wave basis set. Phys. Rev. B *54*, 11169-11186. 10.1103/PhysRevB.54.11169.
7. Perdew, J.P., Burke, K., and Ernzerhof, M. (1996). Generalized Gradient Approximation Made Simple. Phys. Rev. Lett. *77*, 3865-3868. 10.1103/PhysRevLett.77.3865.
8. Ernzerhof, M., and Scuseria, G.E. (1999). Assessment of the Perdew–Burke–Ernzerhof exchange-correlation functional. J. Chem. Phys. *110*, 5029-5036. 10.1063/1.478401 %J The Journal of Chemical Physics.
9. Kresse, G., and Hafner, J. (1994). Norm-conserving and ultrasoft pseudopotentials for first-row and transition elements. J. Phys.: Condens. Matter *6*, 8245. 10.1088/0953-8984/6/40/015.
10. Momma, K., and Izumi, F. (2011). VESTA 3 for three-dimensional visualization of crystal, volumetric and morphology data. J. Appl. Crystallogr. *44*, 1272-1276. 10.1107/S0021889811038970.
11. Chen, F., Wu, J., Wang, D., Xia, Y., Song, Q., Liang, Y., Wang, P., Chen, B., Liang, Y., Yin, Y., et al. (2024). Simultaneous generation of hydroxyl and hydrogen radicals from H+/OH− pairs caused by water–solid contact electrification. Chem. Sci. *15*, 19583-19587. 10.1039/D4SC06227B.